Conditions for conductance quantization in realistic models of atomic-scale metallic contacts

A. M. Bratkovsky, A. P. Sutton, and T. N. Todorov
Department of Materials, University of Oxford, Parks Road, Oxford OX1 3PH, England
(Received 14 February 1995; revised manuscript received 9 May 1995)

We present a comparative analysis of tight-binding and free-electron calculations of the conductance of an atomic-scale metallic contact. The calculations are based on a full dynamic simulation of the atomic structure during the pulloff of the contact, for a range of temperatures. As in previous simulations, we find that the contact evolves through a series of mechanical instabilities and can become highly disordered prior to fracture. Both the mechanical evolution of the contact and the behavior of the conductance depend strongly on temperature. We find that conductance quantization is destroyed easily by irregularities in the shape of the contact and, in the tight-binding model, also in the internal atomic structure of the contact. In the tight-binding calculation conductance quantization is seen only at high temperature, when the contact geometry and structure become very regular. With the free-electron model, we see perfectly quantized conductance plateaus just prior to contact fracture, while the plateaus in the earlier history of the contact are washed out by tunneling. In the free-electron calculation, conductance quantization is seen both at low and at high temperature but is more prominent at high temperature. We use the tight-binding and free-electron results for the conductance to obtain a calibration curve relating the conductance to the constriction width. The calculated conductances lie significantly below the Sharvin limit but the inclusion of the first-order semiclassical correction to the Sharvin formula greatly improves the agreement.

I. INTRODUCTION

Impressive progress in the experimental study of electron transport in quantum nanocontacts has been achieved during the past two years or so with the advent of the mechanically controllable break junction (MCBJ) technique[1,2] and with direct measurements of the conductance using a scanning tunneling microscope (STM) in the contact regime.[3–5] The contacts in these experiments are definitely in the ballistic regime with a large splitting between transverse electron levels ($\sim 0.1-1$ eV). This is large enough for the presence of discrete levels to be reflected in a quantization of the conductance, provided that the longitudinal electron motion is close to adiabatic (i.e., if the constriction is smooth) and provided that the actual atomic structure of the contact is unimportant. There is, as far as we are aware, no direct experimental information about the shape and internal structure of the nanocontacts, and this is why realistic atomistic simulations and conductance calculations have proved invaluable. This lack of experimental information has resulted in a considerable controversy over the question of whether or not conductance quantization may be observed in atomic-scale metallic contacts.

In the early experiments on Pt junctions,[2] clear jumps in the conductance during contact pulloff were found, but these jumps were irregular in size and certainly not quantized in the quantum conductance unit $G_0 = 2e^2/h$. In a realistic theoretical description of these experiments, a tight-binding model was used to calculate the conductance on the basis of a full dynamic simulation of contact pulloff.[6] In this calculation it was seen that during pulloff the contact thins down through a series of abrupt mechanical rearrangements (or instabilities). Each instability was found to result in a corresponding abrupt decrease in the conductance. The values of the conductance between jumps were not quantized, which was explained in terms of irregularities in the atomic topology of the contact. In parallel with this work came further MCBJ experiments on Al, Pt, and Cu,[7] in which generally nonquantized but otherwise very clear and sharp conductance jumps were observed in all three metals. These steps were explained in terms of Ref. 6.

Then, very recently, came a report on the observation of conductance quantization in Pt, Cu, and Ni point contacts in the STM, at room temperature.[3] Also, a free-electron conductance calculation in Ref. 3 on a highly idealized geometry showed quantized conductance steps. The authors of Ref. 3 also raised the question of whether the conductance jumps in this kind of experiment were at all related to mechanical instabilities, or whether they corresponded simply to the closing-off of conductance channels during an otherwise more or less smooth thinning down of the contact. In a response to Ref. 3 it was pointed out[8] first that the experimental observation of conductance quantization is far from universal, and second that the possibility of conductance quantization in these contacts must be analyzed in conjunction with the detailed structure of the contact and that irregularities in this structure may destroy the quantization effect in cases when the idealized jellium model in Ref. 3 would predict it.

In the meantime, there have been experimental observations of quantized conductance plateaus just before contact fracture, in Au contacts, in both low-

temperature[4] and high-temperature[5] STM. Experimental research with the MCBJ technique[9] has revealed prominent conductance quantization for low values of the conductance (i.e., just before contact fracture) in Na, while under the same conditions Pt has shown no signs of the effect. Very recent MCBJ measurements on Au and Cu at room temperature have shown much more pronounced signs of conductance quantization than seen in corresponding low-temperature experiments.[10]

The present work addresses the theoretical aspect of the question of conductance quantization in atomic-scale contacts. The aim is to understand the conditions for the observation of the effect and to elucidate the origin of some of the experimental observations to date. To this end, we have carried out a direct comparison between tight-binding and free-electron conductance calculations on the *same* realistic contact geometry. The contact geometry is generated by a dynamic simulation of the pulloff of a Ni contact. The calculations are done for three different temperatures, 10 K, 150 K, and 250 K, and the effect of temperature on the mechanical response and on the conductance of the contact is investigated.

The essential difference between the two electronic models is that in the free-electron picture the metal is represented by jellium, so that only the *shape* of the contact enters the model, while in the tight-binding picture the exact atomic structure of the contact is reflected explicitly in the Hamiltonian of the system.

We find that conductance quantization does occur, but it requires special conditions and is easily destroyed by the backscattering in realistic geometries. In the tight-binding calculation, conductance quantization can break down both as a result of rapid variation of the contact cross section along the contact and as a result of defects in the internal atomic structure of the contact. With tight binding, we find conductance quantization only at high temperature, when the contact becomes very regular in cross section and in internal structure.

In the free-electron calculation, departures from conductance quantization can occur as a result of insufficient smoothness in the contact *profile*. Conductance quantization is seen only in the late stages of the pulloff, when the narrowest part of the constriction becomes sufficiently smooth in shape. In the earlier stages of the pulloff, distinct conductance plateaus are not seen at all in the free-electron model, due to tunneling effects. In the free-electron calculation, conductance quantization is seen both at low and at high temperature, but is more prominent at high temperature.

The above observations are in agreement with the currently available experimental data. It must be stressed, however, that, to our knowledge, there have been no *systematic* experimental studies of the dependence of the quantization effect on temperature or on the electronic structure of the material.

Finally, we use the tight-binding and free-electron results to obtain a calibration curve relating the conductance to the actual cross-sectional area of the contact. We find a linear relationship between the two in which, however, the conductance is suppressed considerably relative to the Sharvin limit.

II. COMPUTATIONAL METHODS

A. The dynamic simulation

The setup for the atomistic simulations follows closely that in Ref. 6, although the parameters in the simulations were altered. Atomic interactions representing nickel were taken from Ref. 11. These are long-range many-atom interactions of the Finnis-Sinclair form. The total potential energy is expressed as follows:

$$E = \epsilon \left\{ \frac{1}{2} \sum_i \sum_{j \neq i} \left(\frac{a}{r_{ij}} \right)^n - c \sum_i \left[\sum_{j \neq i} \left(\frac{a}{r_{ij}} \right)^m \right]^{1/2} \right\} , \tag{1}$$

where r_{ij} is the distance between atoms i and j, $\epsilon = 1.5707 \times 10^{-2}$ eV, $m = 6$, $n = 9$ and $c = 39.432$, and $a = 3.52$ Å is the fcc lattice parameter. The potential is truncated at $2.001a$, which means that in a perfect fcc crystal there are 140 interacting neighbors to a given atom. We note that with a suitable scaling of the energy and time this potential may also be taken to represent Cu in the same scheme.[11] The functional form in Eq. (1) captures an essential feature of metallic bonding, namely that the strength of a bond increases as the coordination number decreases. This is an important feature in the present context as the coordination of some atoms in the contact decreases from 12 to 2 during the pulloff.

In the simulations the contact geometry is initialized in the following way. The contact consists of a cluster of atoms sandwiched between two slabs. The cluster is obtained by cutting out a cylinder of atoms, with a [111] axis, from a perfect fcc crystal. The cylinder comprises 13 (111) planes, each containing between 19 and 21 atoms. The $...ABC...$ stacking sequence of (111) planes gives rise to a serrated appearance of the sides of the cylinder. There are 265 atoms in the cylinder. This cylinder is attached to the underside of a rectangular slab of 1836 atoms, comprising 6 (111) planes of dimensions $(9a/2)[1,1,-2]$ by $(17a/2)[1,-1,0]$. The cylinder and slab have the same crystal orientations. Periodic boundary conditions are applied in the three orthogonal directions of the slab. The length of the computational cell normal to the slab is such that the cylindrical cluster is in contact with the image slab beneath it as shown in Fig. 1. The computational cell contains 1836+265=2101 atoms.

The simulation at 150 K was carried out first. Initially the system was equilibrated for 5000 time steps of 10^{-14} sec. During this equilibration the area of the slab was allowed to expand but the length of the computational cell normal to the slab was fixed. The length of the computational cell normal to the slab was then reduced gradually by one lattice parameter over 10 000 time steps, in order to simulate the compressive loading that occurs prior to pulloff in the actual experiments. During this reduction of the cell height most of the strain is accommodated predominantly and elastically in the cylinder. This configuration formed the starting point for the pulloff at 150

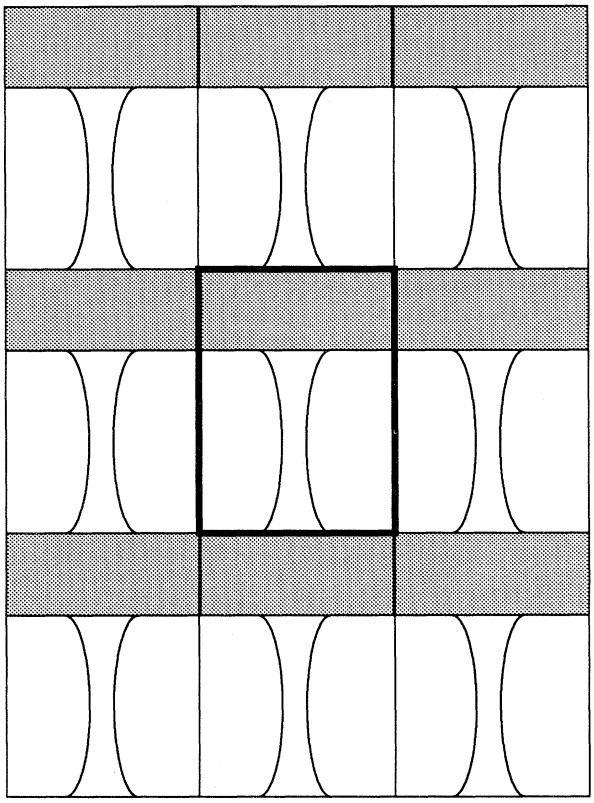

FIG. 1. Schematic illustration of the periodic boundary conditions in the atomistic simulation of the contact pulloff. The central emboldened cell is repeated in three orthogonal directions.

K. For the other two temperatures, 10 K and 250 K, this configuration was annealed for a further 10 000 time steps, at the corresponding temperature, before the start of the pulloff.

The pulloff at all three temperatures was effected at the same constant velocity of $10^{-4}a$ per time step, or 3.52 m/s. In each time step the contents of the computational cell were strained homogeneously normal to the slab such that the cumulative displacement of the top of the cell relative to the bottom was $10^{-4}a$. The strain localizes and becomes inhomogeneous naturally through solving the dynamical equations of motion of the atoms. The Newtonian equations of motion were integrated via the velocity Verlet algorithm,[12] and a Nosé-Hoover thermostat was applied[13] to all atoms in the cell to maintain the temperature at the required value throughout the pulloff. The pulloff was continued until fracture occurred, which required typically 60 000 time steps. Snapshots were recorded every 100 time steps for each run and were used to create a graphical, three-dimensional animation of the pulloff, which made it possible to follow directly the structural evolution of the contact throughout the run.

B. The tight-binding conductance calculation

The tight-binding conductance calculation is implemented in essentially the same way as in Ref. 6. The conductance is calculated at every 10th time step of the pulloff in the dynamic simulation, using explicitly the respective set of atomic coordinates. In general, it was found that the conductance fluctuates rapidly from one geometry to the next, due to the thermal motion of the atoms. These fluctuations have been smoothed out by averaging the calculated conductance over 39 (1 ± 19) successive values before plotting the results. The number 39 has no particular significance: simply, it was found to be large enough for the thermal fluctuations to be washed out, and yet small enough for the gross structure of the conductance curves to be preserved. Note, however, that we have taken the average of the instantaneous conductances, rather than the conductance of an averaged atomic geometry.

Due to the size of the system, no attempt is made to model the true s-d band structure in Ni. Instead, the electronic structure of the contact is represented by an orthonormal nearest-neighbor $1s$ tight-binding model with zero on-site energies and a band-filling of one-half. While this model is not a description of Ni, it makes it possible to trace the connection between the conductance and the atomic topology of the contact and is therefore sufficient for our purposes here.

Furthermore, the calculation of the conductance is always done in the zero-temperature limit. The exact finite-temperature expression for the conductance[14] contains an energy integral, the main contribution to which comes from an energy window of size $\sim kT$ about the Fermi energy E_F. At all three temperatures from the simulations, kT $[\leq 0.02$ eV] is much smaller than the splitting of the transverse electron levels ($\sim 0.1 - 1$ eV) in the contact. For this reason, it is possible to ignore the finiteness of kT and to approximate the conductance by its zero-temperature limit.

In the tight-binding model, the hopping integral H_{ij} between atoms i and j is represented by a function which stays equal to the ideal nearest-neighbor hopping integral up to half-way between first and second neighbors, and then decreases smoothly to zero at second neighbors. Specifically, H_{ij} given by

$$H_{ij} = A \quad \text{for} \quad z_{ij} < z_n,$$
$$H_{ij} = A\frac{1}{2}\left[1 + \cos\pi\left(\frac{z_{ij} - z_n}{z_c - z_n}\right)\right]$$
$$\text{for} \quad z_n \leq z_{ij} \leq z_c, \quad (2)$$

where A is the nearest-neighbor hopping integral in the perfect fcc crystal, z_{ij} is the distance between atoms i and j in units of the ideal nearest-neighbor separation, $z_n = (1 + \sqrt{2})/2$, and $z_c = \sqrt{2}$. The effect of the form of the hopping integral as a function of the separation of the atoms on the calculated conductance is an important and interesting question but it will not be considered here. Our own experience indicates that this effect is quantitative rather than qualitative. For instance, changing

the form of Eq. (2) might alter the size of the thermal fluctuations of the conductance between consecutive geometries. It could also in principle affect slightly the absolute value of the averaged conductance for a given sequence of geometries. We expect, however, that the qualitative effect of the atomic structure and defects in this structure on the conductance will be independent of the precise scaling of the hopping integral.

Periodic boundary conditions are not used in the conductance calculation. Instead, the slabs above and below the tip are replaced by two semi-infinite crystals, labeled 1 and 2, respectively. The atomic positions within the cluster are those given by the simulation. Since the distortion of the slabs in the simulation is negligible, crystals 1 and 2 in the conductance calculation are treated as perfect. We imagine that the cluster atoms are initially decoupled from each other and from the substrate atoms. We then couple the cluster atoms to each other and to the substrate atoms by a coupling V, whose matrix elements are given by Eq. (2). All on-site matrix elements of V are zero.

As is shown in Ref. 14, the zero-voltage, zero-temperature elastic conductance G of the final, coupled system is given by

$$G = \frac{2e^2}{h} 4\pi^2 \mathrm{Tr}[\rho_1^0(E_F) t^\dagger(E_F) \rho_2^0(E_F) t(E_F)], \qquad (3)$$

where $t(E) = V + VG^+(E)V$, $G^+(E)$ is the retarded Green function for the final coupled system, and $\rho_1^0(E)$ and $\rho_2^0(E)$ are the density of states operators for the respective initial separate substrates and are given by

$$\rho_j^0 = \frac{1}{2\pi i}[G_j^{0-}(E) - G_j^{0+}(E)], \quad j = 1, 2. \qquad (4)$$

Here, $G_1^{0\pm}(E)$ and $G_2^{0\pm}(E)$ are the Green functions for the respective separate substrates in the initial decoupled system.

The trace in Eq. (3) is taken in the orthonormal atomic $1s$ basis. The matrix elements of $G_1^{0\pm}(E)$ and $G_2^{0\pm}(E)$ between (111) surface sites on the respective perfect semi-infinite fcc crystals are calculated as in Ref. 14. The matrix elements of $t(E)$ are calculated[6] by solving numerically the Dyson equation

$$t(E) = V + VG^{0+}(E)t(E), \qquad (5)$$

where $G^{0+}(E)$ is defined by its matrix elements $[G^{0+}(E)]_{ij}$ in the atomic basis as follows: $[G^{0+}(E)]_{ij} = [G_1^{0+}(E)]_{ij}$ if $i, j \in$ substrate 1, $[G^{0+}(E)]_{ij} = [G_2^{0+}(E)]_{ij}$ if $i, j \in$ substrate 2, $[G^{0+}(E)]_{ij} = \delta_{ij}/E$ if $i, j \in$ cluster, and $[G^{0+}(E)]_{ij} = 0$ otherwise.

C. Free-electron conductance calculation

Electrons in a quantum constriction are subjected to an ionic (pseudo)potential. In the simplest approximation one ignores its effects and assumes that the electrons are free. This simplification does not affect the classification of states according to the transverse electron motion, but it leaves out the effects of ionic disorder which may be present in real contacts. The ionic disorder can be included in the calculation approximately, as mentioned later in this section. At the same time, the effect of the *shape* of the contact, including atomic roughness, can be treated adequately.

In the present problem, the characteristic length of the contact is smaller than the electron mean-free path, i.e., the contact is ballistic. The linear response theory of transport coefficients then reduces to the much simpler Landauer scattering problem.[15–17] This problem is solved easily within the free-electron approximation and the calculation is orders of magnitude faster than the direct evaluation of the conductance in the tight-binding model [Eq. (3)].

In the present calculation we make use of the fact that the geometry of the contacts from the atomistic simulation is approximately cylindrical. In the free-electron calculation we treat the constriction as a solid of revolution with perfect cylindrical symmetry. While at present this is an approximation, it is interesting to note that in LDA calculations the electronic confining potential for an STM tip in "hollow-site" geometries has been found to have cylindrical symmetry to a good approximation.[18]

The contact profile for the free-electron calculation is obtained from the dynamic simulation in the following way. The longitudinal direction (along the contact) is taken as the x axis. Each atom is treated as a sphere of radius r_0 given by $4\pi r_0^3/3 = v_0/4$, where v_0 is the volume of the fcc unit cell of the bulk material. We define a sampling range Δx and an increment δx along the x axis.

In a given geometry from the simulation, we take a slice of the contact of thickness Δx centered at position x along the contact. From r_0 and the positions of the atomic centers we then find the fractions of all atomic spheres that lie within the slice. Then we equate the total atomic volume contained in the slice to that of a disk of thickness Δx and radius $a_r(x)$. The radius $a_r(x)$ is the effective radius of the contact at x. The slice is then moved along by the increment δx and the procedure is repeated, producing the effective radius of the contact at position $x + \delta x$, $a_r(x + \delta x)$. At the end of the procedure, we have a profile for the contact given by the effective radius $a_r(x)$ as a function of the coordinate x along the contact.

The smoothness of the profile depends on the sampling range Δx. For the moment, Δx is set equal to d_{111}, the ideal separation between neighboring fcc (111) planes. With this choice of Δx, the contact profile captures the surface roughness due to variations in the numbers of atoms between neighboring atomic layers in the contact, but does not include any corrugation due to the surface atoms themselves. The increment δx is set equal to $\frac{1}{10} d_{111}$.

We treat the roughness perturbatively, according to Ref. 20. To this end, we define a smooth profile $a(x)$ by

$$a(x) = \int_{-\infty}^{\infty} a_r(x - x') f(x') dx', \qquad (6)$$

where $f(x) = \gamma/\pi(x^2+\gamma^2)$ is the normalized Lorentzian with width $\gamma = 2d_{111}$. Then the roughness of the profile is by definition

$$\xi(x) = a_r(x) - a(x). \tag{7}$$

As discussed in the context of the tight-binding calculation, we may ignore the finite-temperature smearing of the Fermi-Dirac function. The conductance G of our system is thus given by the zero-temperature Landauer formula[15,16]

$$G = \frac{2e^2}{h}\sum_{ab} T_{ab}(E_F), \tag{8}$$

where $T_{ab}(E) = t_{ab}(E)t^{\star}_{ab}(E)$ is the transmission coefficient for an electron incident on the contact from the left in mode (channel) a and transmitted into mode b on the right, at the Fermi energy. The different modes are simply the different eigenstates of the transverse electron motion. The total number of propagating modes is $N \sim k_F^2 A$, where k_F is the Fermi wave vector and A is the cross-sectional area of the contact.

The calculation of the conductance in this approach requires the solution of the Schrödinger equation to find the transmission coefficients. Assuming an infinite square well for the confining electron potential, we have to solve the Schrödinger equation

$$-\frac{\hbar^2}{2m^*}\left(\frac{\partial^2}{\partial x^2}+\frac{\partial^2}{\partial y^2}+\frac{\partial^2}{\partial z^2}\right)\psi(x,\mathbf{r}) = E\psi(x,\mathbf{r}), \tag{9}$$

with the boundary condition $\psi[|\mathbf{r}| = a_r(x)] = 0$, where $\mathbf{r} = (y,z)$ is the transverse component of the position vector. It is worth noting that the requirement that the wave function should vanish at the constriction walls corresponds precisely to the boundary conditions implied in the tight-binding calculation.

We reduce the problem to that of solving the Schrödinger equation for the contact with the smooth profile $a(x)$ by a simple canonical coordinate transformation.[20] This transformation introduces an effective bulk perturbation $\hat{V}_\xi(x,\mathbf{r})$ into the Schrödinger equation (9) which now takes the following form:

$$-\frac{\hbar^2}{2m^*}\left(\frac{\partial^2}{\partial x^2}+\frac{\partial^2}{\partial y^2}+\frac{\partial^2}{\partial z^2}+\hat{V}_\xi(x,\mathbf{r})\right)\psi(x,\mathbf{r}) = E\psi(x,\mathbf{r}), \tag{10}$$

with the boundary condition $\psi[|\mathbf{r}| = a(x)] = 0$.

The perturbation due to the roughness $\xi(x)$ is approximately given by[20]

$$\hat{V}_\xi(x,\mathbf{r}) = -\frac{2\xi(x)}{a(x)}\hat{T}_r, \tag{11}$$

where

$$\hat{T}_r = -\frac{\hbar^2}{2m^*}\left(\frac{\partial^2}{\partial r^2}+\frac{1}{r}\frac{\partial}{\partial r}+\frac{1}{r^2}\frac{\partial^2}{\partial\phi^2}\right) \tag{12}$$

is the transverse part of the total kinetic energy operator, and (r,ϕ) are the polar coordinates in the transverse (y,z) plane.

We solve Eq. (10) by separating the "fast" transverse motion from the "slow" longitudinal motion of the electron:

$$\psi(x,\mathbf{r}) = \sum_{m\alpha}\chi_{m\alpha}(x)u^x_{m\alpha}(\mathbf{r}), \tag{13}$$

where $u^x_{m\alpha}(\mathbf{r})$ is a solution of the radial equation of motion

$$\hat{T}_r\, u^x_{m\alpha}(\mathbf{r}) = \epsilon_{m\alpha}(x)u^x_{m\alpha}(\mathbf{r}) \tag{14}$$

with the boundary condition $u^x_{m\alpha}[|\mathbf{r}| = a(x)] = 0$, and has the following form:

$$\begin{aligned} u^x_{m\alpha}(\mathbf{r}) &= C_{m\alpha}J_{|m|}(\kappa_{m\alpha}r)e^{im\phi}, \qquad m = 0,\pm1,..., \\ C_{m\alpha} &= \frac{1}{\sqrt{\pi}a(x)J_{|m|+1}(\gamma_{|m|\alpha})}, \\ \kappa_{m\alpha} &= \gamma_{|m|\alpha}/a(x), \quad \epsilon_{m\alpha}(x) = \frac{\hbar^2\kappa^2_{m\alpha}}{2m^*}, \end{aligned} \tag{15}$$

where $\gamma_{m\alpha}$ is the αth root of the Bessel function $J_m(x)$. These equations define the modes which will be populated up to the Fermi level and contribute to the conductance.

Substituting Eq. (13) in Eq. (10), multiplying it by $\bar{u}^x_{k\beta}$, and integrating over the cross section area at the given x we obtain the following system of equations:

$$\left[\frac{d^2}{dx^2}+\kappa^2-\left(1-\frac{2\xi(x)}{a(x)}\right)\kappa^2_{m\alpha}(x)\right]\chi_{m\alpha}(x) = -\sum_{k\beta}\left(2A_{m\alpha k\beta}(x)\frac{d}{dx}+B_{m\alpha k\beta}(x)\right)\chi_{k\beta}(x), \tag{16}$$

where $\kappa^2 = 2m^*E/\hbar^2$, and the terms on the right-hand side correspond to nonadiabatic mode mixing processes,

$$A_{m\alpha k\beta}(x) = \int_0^{a(x)} r\,dr \int_0^{2\pi} d\phi\ \bar{u}^x_{m\alpha}(\mathbf{r})\frac{\partial}{\partial x}u^x_{k\beta}(\mathbf{r}), \tag{17}$$

$$B_{m\alpha k\beta}(x) = \int_0^{a(x)} r\,dr \int_0^{2\pi} d\phi\ \bar{u}^x_{m\alpha}(\mathbf{r})\frac{\partial^2}{\partial x^2}u^x_{k\beta}(\mathbf{r}). \tag{18}$$

Equations (10) and (16) are exactly equivalent. No approximation has been made in writing the wave function in the form (13). The nonadiabatic terms A and B contain the parameters $a'(x)$ and $a(x)a''(x)$, where the primes stand for the derivative d/dx. In realistic geometries adiabaticity is poorly obeyed and therefore we have retained the nonadiabatic terms.

It is, however, very instructive to consider also the ideal case of smooth geometries with $\sqrt{|a''a|} \ll 1$ (adiabatic contact), when the nonadiabatic terms can be neglected, allowing an analytical solution of the problem.[22] In the semiclassical regime an electron emitted from the left terminal and traversing the smooth contact experiences an adiabatically varying potential. If an electron propagat-

ing in the mode $m\alpha$ has positive kinetic energy everywhere in the contact, $E > \epsilon_{m\alpha}$, it will be transmitted to the right. If this condition is violated the transmission amplitude to the right will be exponentially small, in other words the electron will be backscattered. This allows a simple classification of electron states as belonging to open or closed channels. The conductance of the adiabatic contact will then be

$$G = \frac{2e^2}{h} \sum_{m\alpha} \theta \left[\epsilon_F - \epsilon_{m\alpha}(a_{\min}) \right], \tag{19}$$

where $\theta(x) = 1$ when $x > 0$, and zero otherwise, ϵ_F is the Fermi energy, and $a_{\min}$ is the minimal constriction radius. Equation (19) means that electronic states with $\gamma_{m\alpha} \leq k_F a_{\min}$ will belong to open channels, compared to the total number of channels entering the opening of the constriction with radius a_∞, $\gamma_{m\alpha} \leq k_F a_\infty$, where a_∞ is the radius of the opening.

Equation (19) describes the conductance staircase which has been observed experimentally in a two-dimensional electron gas (2DEG) subject to a split-gate voltage.[21] The cylindrical symmetry of our contacts gives rise to an orbital degeneracy of the wave functions. The height of the corresponding conductance steps could be either G_0 or $2G_0$ depending on the sequence of the Bessel function roots.[19] This degeneracy will be *lifted* when the constriction is not exactly cylindrically symmetric, and then one will have only conductance steps of height G_0, as discussed in detail in Ref. 20. In nonadiabatic situations, tunneling in channels which are just opening will tend to smear out the sharp conductance steps.[22]

It is important now to define the possible reason for the breakdown of conductance quantization in real nanoconstrictions. The Landauer formula, Eq. (8), suggests that this reason is the backscattering of electrons. In STM and break-junction devices *direct* backscattering from the rough (nonadiabatic) contact surfaces and/or internal structural disorder is the prime candidate for the mechanism of departures from conductance quantization, because the variation in the electronic potential due to such defects has a characteristic length scale that is comparable to the Fermi wavelength of the electrons. The effects of internal disorder can in principle be included in the free-electron formalism phenomenologically as a bulk perturbation in addition to V_ξ, Eq. (11).

This is in stark contrast to what happens in homogeneous and *smooth* contacts. There, direct backscattering is ineffective. In such contacts, mode mixing, which requires much smaller deviations from adiabaticity than backscattering, may still be present, but this mode mixing conserves the total conductance and does not lead to a breakdown of conductance quantization, as has been seen in numerical calculations.[23] This result is a consequence of the unitarity of the scattering S matrix.[24]

In such contacts the *indirect* backscattering via *quasibound* states becomes important although it is formally a second-order effect.[25] Quasibound states may appear, for instance, as a result of a local widening of the contact, as we will see later. The indirect backscattering involves a mode-mixing process in which an electron in a propagating mode undergoes scattering into the quasibound state with a corresponding suppression of the conductance.

Quasibound states may also result in the opposite effect — an enhanced conductance due to resonant tunneling in a nonpropagating mode via the quasibound state.[25] We will discuss a specific example of this effect in the following section.

The Appendix contains a brief review of the general relation between the continuous model used in the free-electron calculation and the discrete tight-binding model discussed earlier.

III. RESULTS AND DISCUSSION

A. 10 K results

Figure 2 shows the tight-binding (TB) and free-electron (FE) conductance curves, and the minimal contact diameter, $2a_{\min}$, in units of the Fermi wave vector, throughout the pulloff of the contact at 10 K. At the bottom of the figure there are plots of the contributions to the conductance from individual conductance channels (some of which are doubly degenerate) in the free-electron model. The horizontal axis represents the number N of the time step from the simulation, in units of 100.

We can immediately make one important observation, namely that as far as the *rough magnitude* of the conductance is concerned, the tight-binding and the free-electron results are quite similar. At the same time, the detailed structure of the two curves is rather different.

The TB conductance curve exhibits the same abrupt jumps as the ones reported in Ref. 6. Each jump coincides with an abrupt mechanical rearrangement, or instability, in the contact.

All mechanical instabilities result in an elongation of the contact by one atomic layer and in a corresponding decrease in the contact cross section. These sudden reductions in cross section correspond to the abrupt jumps in the minimal contact diameter $2a_{\min}$ from the FE calculation.

In general, during a mechanical rearrangement the contact suddenly loses its ordered structure, undergoes some internal restructuring, and then reorders in its new, longer, and thinner geometry. We have observed two different kinds of mechanical instability. The first is seen in the early stages of the pulloff when the contact cross section is relatively large. The contact remains essentially crystalline and the instability involves the nucleation and glide of a dislocation on an inclined (111) slip plane. In the present model, where the stacking fault energy is zero, the dislocation is dissociated into Shockley partials. The first Shockley partial glides completely through the contact creating a stacking fault on the inclined slip plane. After a further short period the second partial glides along the same path and removes the stacking fault. The final result is that the contact has lengthened by one (111) plane, and it is slightly narrower.

The second kind of instability is seen in the later stages of the pulloff when the constriction is relatively narrow.

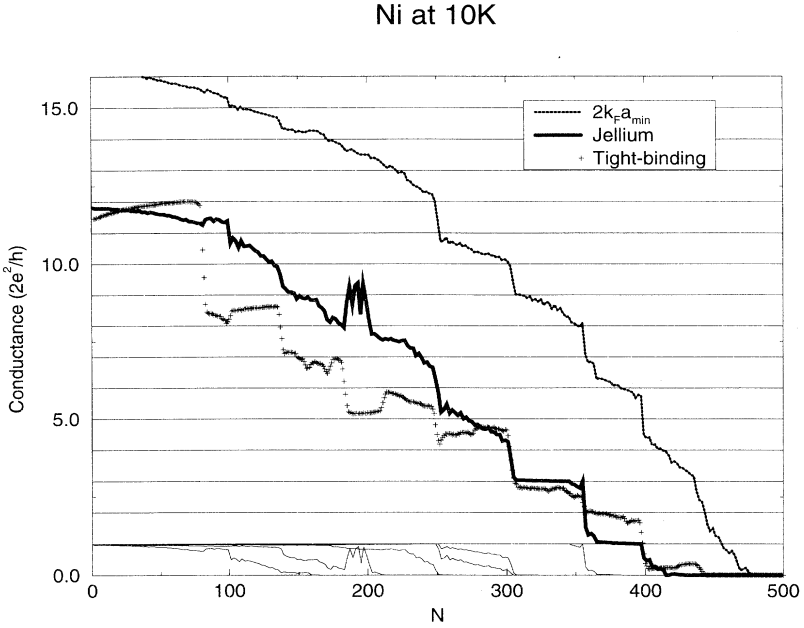

FIG. 2. The tight-binding and the free-electron conductances, in units of $2e^2/h$, and the minimal contact diameter $2a_{\min}$, in units of the Fermi wave vector, during the pulloff of the contact at 10 K. N (the horizontal axis) is the time step from the simulation in units of 100. The contributions of individual conductance channels in the free-electron model are shown at the bottom of the plot. Observe the opposing behavior of the two conductances between $N \approx 180$ and $N \approx 205$.

In this case several atomic layers in the vicinity of the narrowest part of the contact become highly disordered, so much so that it is impossible to distinguish layers anymore. The onset of this disordering transition is very abrupt, and it is completed in a few hundred time steps, during which the constriction reorders and one more layer appears. In this process the formation of the new layer is more homogeneous than in the first kind of instability, in that it involves a substantial *volume* centered at the constriction rather than glide on a single inclined *plane*.

Between instabilities, the contact elongates elastically, which is reflected in a uniform decrease in $a_{\min}$ between the abrupt jumps. The total elastic elongation of the contact between instabilities is typically of the order of the bond length. This is a universal feature of all of our simulations. It follows from the very essence of the instabilities as processes in which the contact elongates by one atomic layer at a time.

The slight positive slopes of the first couple of TB conductance plateaus are due to the recovery of the bonds from the elastic compression of the contact preceding the pulloff. Apart from that, the TB conductance generally stays constant between jumps. The values of the conductance at these plateaus, however, are not quantized in units of G_0, and neither are the actual jumps. This is due to the fact that both the number of atoms and the atomic geometry vary substantially between successive atomic layers in the contact. This lack of uniformity destroys the translational invariance of the system (or of the TB Hamiltonian), prevents the appearance of well-defined conductance channels (or transverse modes) in the TB electronic structure, and gives rise to backscattering.

Right before fracture, between about $N = 400$ and $N = 450$, the narrowest part of the contact begins to deviate substantially from the normal fcc crystalline structure, as shown in Fig. 3. A nominally one-atom contact exists at that stage, but this one-atom contact is a highly defective one. There is a significant variation in the bond lengths and in the coordination numbers of the atoms in the narrowest part of the contact. In the TB model, this disorder results in strong backscattering and the TB conductance is only a fraction of G_0, the value that may be

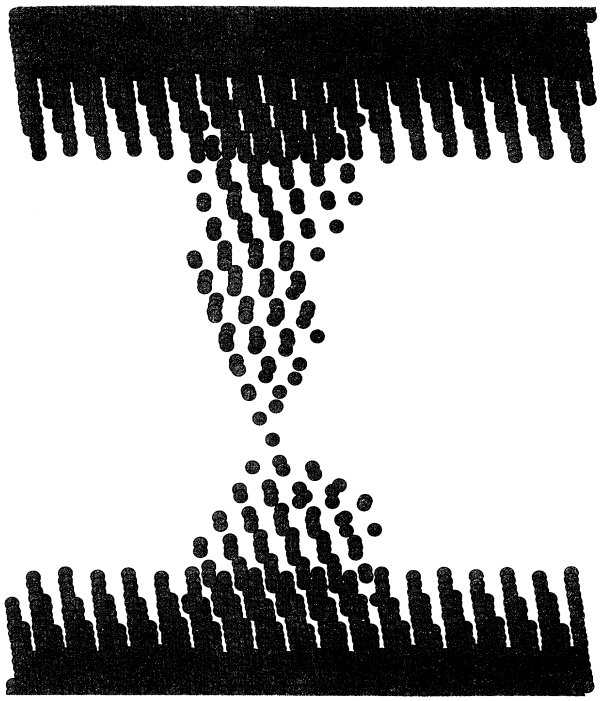

FIG. 3. The contact at $N = 415$ in the 10 K simulation. The snapshot is tilted in order to make it easier to see the internal structure. Note the irregularity in the bond lengths and in the coordination numbers in the narrowest part of the contact.

expected for a perfect one-atom contact.[14]

Now we turn to the FE curve. Its most prominent feature are the flat quantized plateaus at $G = 1G_0$ and $G = 3G_0$. They correspond to the last two transverse modes of the circular constriction. The latter mode is doubly degenerate. The actual jumps delimiting these two plateaus still correspond to sudden reductions in cross section due to mechanical instabilities, much like the jumps in the TB curve.

No other clear conductance plateaus are present in the FE curve. An inspection of the channel-by-channel contribution to G shows that in the early stages of the pulloff, the conductance channels do not get closed off abruptly, but rather more gradually, over broad ranges of N values. This may be explained in terms of tunneling. As a result of the nonadiabatic variation of the effective constriction diameter along the contact, individual channels continue to conduct for some time after the effective one-dimensional (1D) potential barriers for them have risen above E_F, by tunneling through these barriers. Thus, the gradual decrease in the minimal contact diameter during the elastic elongation of the contact between instabilities causes a gradual decrease in the FE conductance between the jumps, and hence the absence of flat conductance plateaus in the FE curve in the early stages of the simulation. In the late stages of the pulloff the profile of the narrowest part of the contact becomes much smoother and closer to adiabatic than before. Tunneling now becomes insignificant and individual conductance channels are either fully open or fully closed, hence the flat quantized plateaus before fracture.

Interestingly, the TB curve shows clear, more or less constant conductance plateaus between instabilities even in the early stages of the pulloff, where the FE curve shows none. This difference between the two models is subtle and important. During the elastic elongation of the contact between instabilities successive atomic layers in the contact are pulled farther apart while neighboring atoms within each layer move closer together. Now, in the TB model the effective cross section of the contact is determined mainly by the number of atoms in a given atomic layer. Variations in the *bond lengths* within the layer have a secondary effect on the TB conductance. Since the atomic structure of the contact does not change between instabilities but only the bond lengths do, in the TB model the effective minimal cross section between instabilities stays more or less constant and hence the flat TB conductance plateaus.

A very instructive difference between the TB and the FE curves occurs between $N \approx 180$ and $N \approx 205$, when on the FE curve there is a prominent *peak*, while on the TB curve there is a *trough*. The FE peak comes from a corresponding peak in the contribution to G of one particular channel, as may be seen from the bottom of Fig. 3. This channel starts closing off slowly at around $N = 100$, and then, after it has closed down almost completely, it reopens temporarily between $N \approx 180$ and $N \approx 205$, giving rise to the peak. The reason may be understood by an inspection of Fig. 4, which shows a series of contact profiles for the N range of interest. As may be seen from these profiles, over that part of the pulloff the narrowest point of the contact moves from one position along the contact to another. During this process, there is a stage when the contact is a symmetric double constriction. This geometry corresponds to symmetric 1D double barriers in the effective 1D potentials for the various channels. These double barriers harbor quasibound states, and when the energy of one of these states passes the Fermi energy, electrons in the respective channel experience resonant tunneling with a greatly enhanced contribution to G.[25] Thus, the origin of the FE peak in Fig. 3 is resonant tunneling.

Let us now consider the trough in the TB curve. An inspection of the actual atomic geometry from the dynamic simulation reveals (Fig. 5) that over the corresponding N range, there is a persistent crystal defect in the contact. This crystal defect is a stacking fault, running straight across the whole contact. The presence of this defect makes no difference in the FE calculation. However, in the TB calculation, this defect leads to a further loss

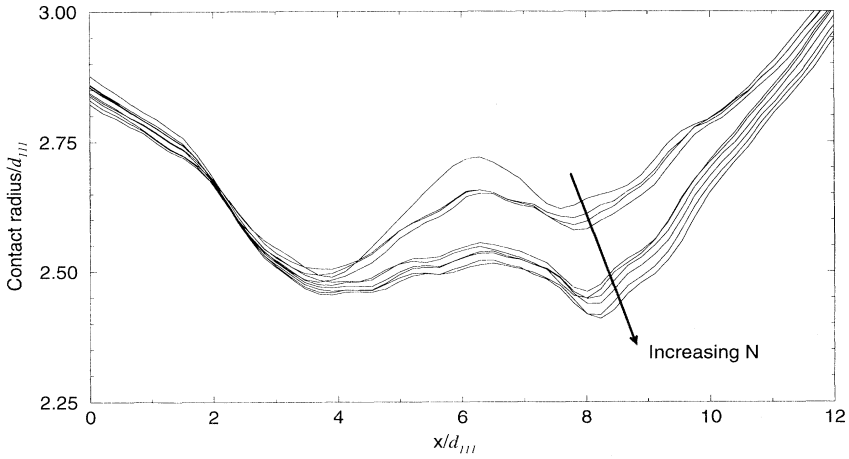

FIG. 4. A series of contact profiles between $N \approx 180$ and $N \approx 205$ in the 10 K simulation. The contact radius and the longitudinal position x along the contact are given in units of d_{111}, the ideal separation between (111) fcc layers. Observe the temporary appearance of a nearly symmetric double constriction.

FIG. 5. The contact at $N = 193$ in the 10 K simulation. Observe the stacking fault (indicated by the arrows) running across the contact. This stacking fault gives rise to the scattering responsible for the trough in the tight-binding conductance.

of translational invariance in the Hamiltonian, which in turn gives rise to increased scattering. This scattering suppresses the conductance and gives rise to the trough.

B. 150 K results

The results of the 150 K calculations are shown in Fig. 6. During the early stages of the pulloff, the mechanical behavior of the contact and the TB and FE conductances show essentially the same features as in the 10 K case. An interesting feature in the TB conductance curve, which is present at all three temperatures but is most prominent here, are the distinct dips just after a conductance jump and just before the following plateau. The origin of these dips is the following. As discussed before, the onset of a mechanical instability is marked by the sudden loss of the normal ordered atomic structure in the contact. This is when the jump in the TB conductance occurs. The TB conductance stays at its value just after the jump while the disorder in the contact persists. When the atomic rearrangement is finally completed, the contact recovers its normal crystalline structure and settles into its new geometry. The recovery of crystallinity in the contact leads to a slight rise in the conductance relative to the preceding disordered situation, and so the plateau at which the conductance eventually settles is a bit higher than the value of G just after the onset of the instability. This gives rise to the apparent conductance dips. There are no corresponding dips in the FE curve, because the loss of crystallinity has no effect on the FE Hamiltonian.

In the present 150 K simulation the contact loses its crystalline structure *permanently* at a rather early stage of the pulloff—at about $N = 250$. From that point on, the narrowest part of the contact is more liquidlike than solidlike. The departure from crystallinity is so high that there are no well-defined atomic layers in a sizeable section of the contact (Fig. 7).

There are no more clear mechanical instabilities and the cross section of the contact decreases gradually rather than in discrete steps, with the exception of a single event around $N = 420$ when some rearrangement in the disordered region takes place. This mechanical behavior is reflected in the TB curve, which for $N \geq 250$ is irregular and without distinct jumps or plateaus.

At the same time, the *profile* of the contact is now quite smooth. As a result of that, the FE curve shows two

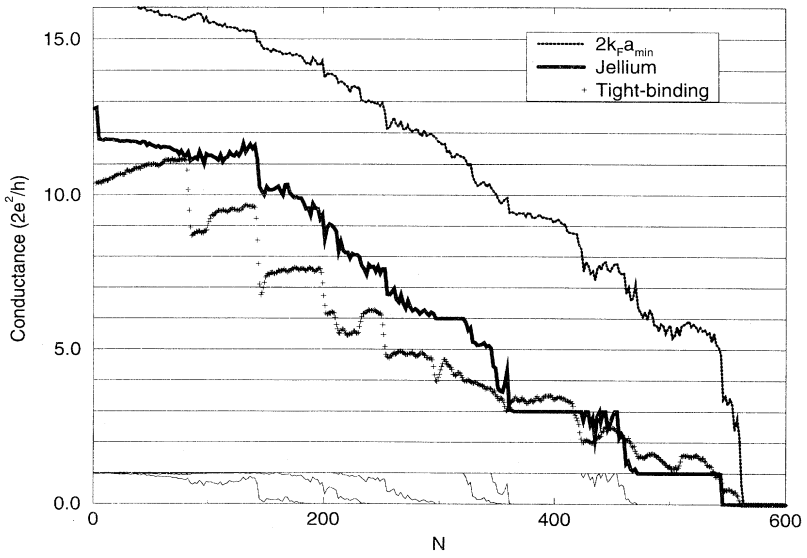

FIG. 6. The tight-binding and the free-electron conductances, in units of $2e^2/h$, and the minimal contact diameter $2a_{\min}$, in units of the Fermi wave vector, during the pulloff of the contact at 150 K. N (the horizontal axis) is the time step from the simulation in units of 100. The contributions of individual conductance channels in the free-electron model are shown at the bottom of the plot.

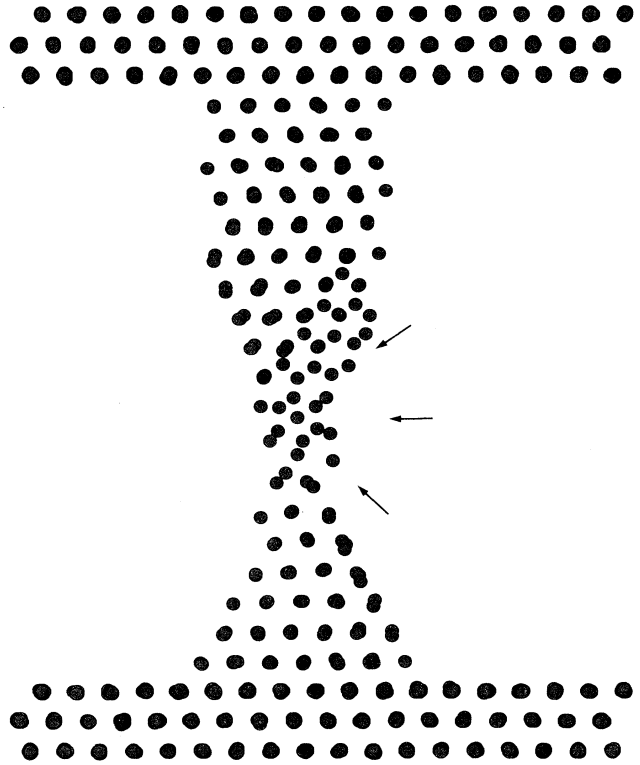

FIG. 7. The contact at $N = 470$ in the 150 K simulation. A section of the constriction (indicated by the arrows) has become highly disordered and smooth in profile.

long flat quantized plateaus, at $G = 1G_0$ and $G = 3G_0$, and some hint at a quantized plateau at $G = 6G_0$. The abrupt conductance jumps delimiting these plateaus do not result from sudden reductions in cross section, but follow from the sudden pinching off of conductance channels during a gradual thinning down of the smooth contact profile. Thus, when the contact profile is sufficiently smooth, in the FE model it is possible to have abrupt and quantized conductance jumps without abrupt reductions in cross section. This is an example of conductance jumps that are not related to mechanical instabilities.

Interestingly, the drop in cross section around $N = 420$ damages slightly the FE conductance plateau at that point, but does not lead to a conductance jump. The splitting of the transverse energy levels in the narrow constriction is quite large and the reduction in the contact diameter is not sufficient to pinch off a channel. This is an example of an abrupt jump in cross section which does *not* generate a corresponding conductance jump.

C. 250 K results

The 250 K results are presented in Fig. 8. Both the TB and the FE conductance curves are substantially different from before. Unlike before, most of the plateaus on the TB curve are in fact at quantized conductance values (integer multiples of G_0). Also unlike before, the FE curve now shows three, as opposed to just two, prominent quantized plateaus, the first one of which occurs fairly early in the pulloff and has the high conductance value of $6G_0$.

The origin of these features lies in the mechanical evolution of the contact during the pulloff. Due to the higher kinetic energy of the atoms, it is now possible for the contact to undergo larger overall structural rearrangements than before. At any temperature, the contact would tend to decrease its total surface area for a given contact volume. (Atoms on the surface are less tightly bound than bulk atoms, and this gives rise to a surface energy. Thus, decreasing the surface area also decreases the total energy.) The difference from the previous two temperatures is that now there is enough kinetic energy in the contact to enable it to pursue this tendency to minimize its surface area. In an animation of the simulation we

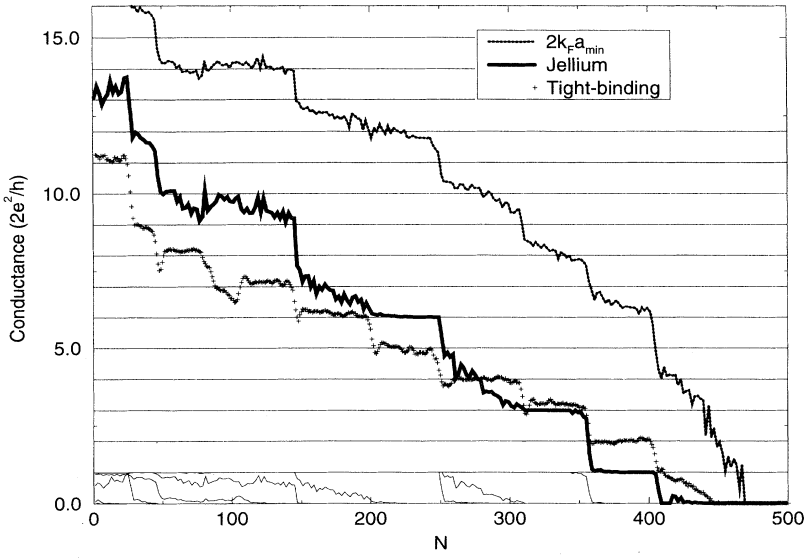

FIG. 8. The tight-binding and the free-electron conductances, in units of $2e^2/h$, and the minimal contact diameter $2a_{\min}$, in units of the Fermi wave vector, during the pulloff of the contact at 250 K. N (the horizontal axis) is the time step from the simulation in units of 100. The contributions of individual conductance channels in the free-electron model are shown at the bottom of the plot.

FIG. 9. The contact at $N = 220$ in the 250 K simulation. Layers 4 to 8 (indicated by the arrows) from the bottom of the contact have nearly identical atomic geometries.

see that as a result of the first two instabilities, the contact acquires a geometry in which all atomic layers within the contact are very similar to each other. The middle section of the contact represents a region several atomic layers long, in which there is hardly any variation at all in the numbers of atoms or in the atomic geometry of the layers (Fig. 9). This translationally invariant piece of the contact allows the formation of well-defined conductance channels in the TB model and is the origin of the quantization of the TB conductance plateaus. The improved uniformity of the contact cross section is also the reason for the larger number of flat quantized plateaus in the FE curve.

In the present simulation the contact remains crystalline almost until the very end, as in the 10 K case. The early loss of crystallinity at the intermediate temperature of 150 K can be seen as a sign of an overall lack of stability of the contact at that temperature (and strain rate), in the sense that there already is enough kinetic energy in the contact to allow the initiation of much more substantial atomic rearrangements than at 10 K, and yet this kinetic energy is not sufficient to enable the contact to complete these rearrangements and recover its crystallinity, as it can do at 250 K.

D. Effects of atomic surface corrugation

In all of the FE calculations so far, the sampling range Δx used to extract the jellium profile from the real atomic geometry has been set equal to the separation d_{111} between neighboring fcc (111) layers. The calculated effective contact radius is thus averaged over atoms from neighboring layers and does not have any atomic-scale corrugation. Now we wish to study the effects on the conductance of variations in the contact radius due to individual atoms on the surface. For this purpose we set Δx equal to half the (111) layer spacing and obtain a profile with a corresponding atomic corrugation. Figure 10 shows a comparison between a profile with $\Delta x = \frac{1}{2}d_{111}$ and a profile with $\Delta x = d_{111}$ for the same contact (the one from Fig. 5). We use the 10 K simulation to compare the FE results for the conductance with and without this corrugation in place.

The respective FE conductance curves for the 10 K run are shown in Fig. 11. As may reasonably be expected, the additional surface roughness in the case with the corrugation leads to an overall suppression of the conductance relative to the case without the corrugation. Only one of the two quantized plateaus found before is present now. Also, the resonance peak around $N = 200$ has sustained some damage, even though it has survived.

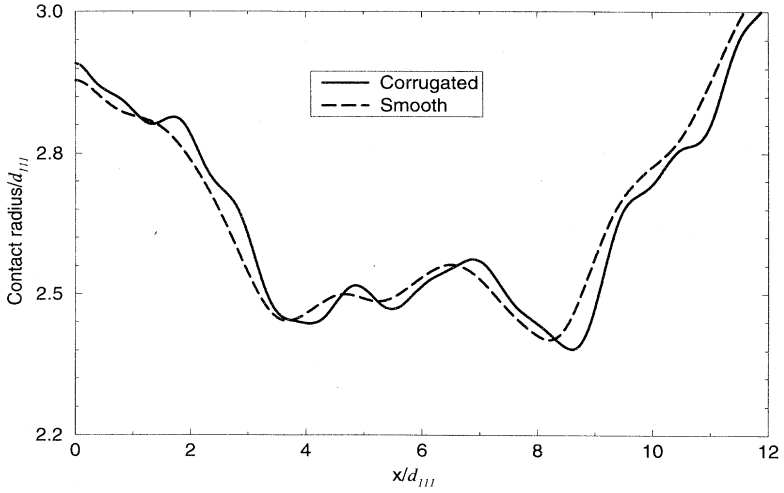

FIG. 10. Comparison between a contact profile obtained with $\Delta x = \frac{1}{2}d_{111}$, showing atomic corrugation due to the surface atoms, and a smoother profile obtained with $\Delta x = d_{111}$. Both profiles refer to the contact from Fig. 5.

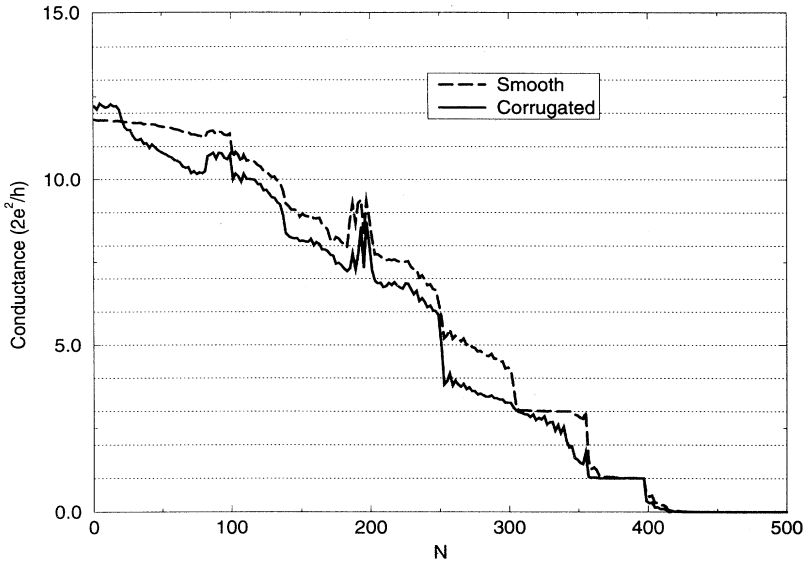

FIG. 11. A comparison of the free-electron conductances for the 10 K simulation calculated with and without atomic corrugation ($\Delta x = \frac{1}{2}d_{111}$ and $\Delta x = d_{111}$, respectively). N (the horizontal axis) is the time step from the simulation in units of 100.

IV. CONCLUSIONS

We have calculated the electronic conductance throughout the pulloff of an atomic-scale metallic contact using both the free-electron (jellium) model and a $1s$ nearest-neighbor tight-binding model. We have also studied the effect of temperature on the mechanical behavior and thereby on the conductance of the contact.

The principal difference between the two electronic models is that in the free-electron model the conductance is determined solely by the profile of the contact, while in the tight-binding model, the Hamiltonian and hence the conductance depend on the precise atomic structure of the contact. This difference becomes particularly important in situations when the contact develops structural defects.

In reality, no system will be completely FE-like or completely TB-like. On the one hand, jellium may not be an entirely accurate representation of FE metals on the size scale of interest here. On the other hand, most metals with a TB-like band at the Fermi energy also have an FE-like s band at the Fermi energy. Thus, the correct description of most real systems is likely to fall somewhere between the two extremes. The results in the present paper should be taken as a qualitative indication of trends which might prevail in various cases, and not as a direct quantitative theory of specific real systems.

In conclusion, we address four points.

A. Conditions for the observation of conductance quantization in atomic-scale contacts

Good conductance quantization (CQ) can be expected only in smooth and homogeneous constrictions, in systems of any dimensionality. The origin of CQ lies in the fact that electron transmission in such constrictions is reflectionless.[22] In general, the reason for the breakdown of CQ in imperfect constrictions is electron *backscattering.*

Our results show that the main mechanism for departures from CQ in a real atomic-scale contact is the *direct* backscattering off (i) nonadiabatic surfaces and (ii) internal structural defects. Such backscattering is responsible for the experimentally observed presence both of conductance plateaus at noninteger conductance values and of conductance jumps of noninteger size. We emphasize that multiple scattering and mode mixing are included fully in both the TB and the FE calculation schemes.

Our calculations show that the mechanical behavior of the contact and hence the conditions for the observation of CQ depend on temperature. At low temperature, there can be substantial variation in the number of atoms and in the atomic geometry of successive atomic layers in the contact. The nonadiabaticity of the constriction prevents CQ with both the FE and the TB models. With the FE model, suitable conditions for CQ appear only towards the end of the pulloff, when the narrowest part of the constriction becomes sufficiently smooth in profile. This results in the appearance of some quantized plateaus in the FE conductance just before fracture. In the TB model, the large departures from crystalline periodicity prior to fracture only make matters worse than before. Thus, at low temperature CQ is seen only with the FE model, and only in the last stages of the pulloff.

At high temperature, CQ is seen with both models. The kinetic energy of the atoms at high temperature enables the contact to undergo substantial restructuring and to acquire a much more regular geometry than before. In pursuit of minimizing its surface area, the contact develops a middle section consisting of several nearly identical consecutive layers of atoms. This translationally invariant section of the contact results in the appearance of quantized plateaus in the TB conductance. The presence of a long smooth neck of constant cross section has a wholesome effect on the FE conductance too. The

quantized plateaus on the FE conductance curve are now more in number and go up to higher conductance values than at low temperature.

We may thus say that with both models the conditions for observing CQ are more favorable at high temperature than at low temperature. With TB, CQ is present only at high temperature. With the FE model, CQ is present in both temperature regimes, but is more prominent at high temperature, and is likely to be seen only in the late stages of the pulloff.

These results agree with the existing experimental observations. Low-temperature MCBJ experiments on Pt, a highly non-FE metal, have revealed no signs of CQ,[9] while room-temperature STM measurements on Pt have shown signs of the effect.[26] Low-temperature MCBJ studies on Na, which is a highly FE-like metal, have shown prominent CQ for low conductance values, just before contact fracture, while for higher conductance values the signs of the effect are weaker or absent.[9] According to some very recent MCBJ research, high-temperature measurements on Au and Cu have shown much clearer signs of CQ than low-temperature measurements.[10]

B. Origin of the conductance jumps

It is sometimes asked whether the conductance jumps that are seen experimentally during contact pulloff are due to abrupt decreases in the contact cross section or whether they are due to the abrupt pinching off of conductance channels during a smooth decrease in the cross section. Our results show that there is a variety of possibilities enumerated below.

When the geometry of the contact is not sufficiently uniform to allow CQ, then each mechanical instability results in a nonquantized conductance jump. In the present calculations this is seen with both electronic models in the early stages of the pulloff at low temperature.

When the constriction is sufficiently uniform for the conductance to be quantized (an integer multiple of G_0), then abrupt reductions in cross section due to instabilities may give rise to quantized conductance jumps, as this happens in the TB calculation at 250 K, or they could result in no conductance jumps, as this happens around $N = 420$ in the 150 K FE calculation.

It is also possible to have quantized conductance jumps which do not correspond to any instabilities. This happens for instance in the 150 K FE calculation. The quantized FE conductance jumps in the regime when the constriction is disordered and smooth in profile correspond to the sudden pinching off of conductance channels during an otherwise gradual thinning down of the contact.

C. Calibration of the conductance

Using conductance measurements as a means of determining the cross-sectional area of an atomic-scale contact is an attractive idea. Its implementation, however, requires a prescription for relating a given measured conductance to a given contact area. Our results make it possible to obtain a calibration curve relating these two quantities.

Figure 12 contains plots of the calculated tight-binding and free-electron conductances for all three temperatures versus the dimensionless parameter $(k_F a_{\min})^2$, where k_F is the Fermi wave vector and $a_{\min}$ is the effective minimal contact radius. The Sharvin limit, $G_S = G_0(k_F a_{\min})^2/4$,[27] is also shown for comparison and it is easy to see that it significantly overestimates both the FE and TB conductances.

Even in the case of perfectly adiabatic jellium constrictions, the actual conductance always lies below the Sharvin value.[20,28] The reason is that, at least in the case of hard-wall constrictions, the Sharvin formula overcounts the number of propagating modes for a given minimal cross section. Correct counting, which takes into account the fact that the electron wave functions vanish

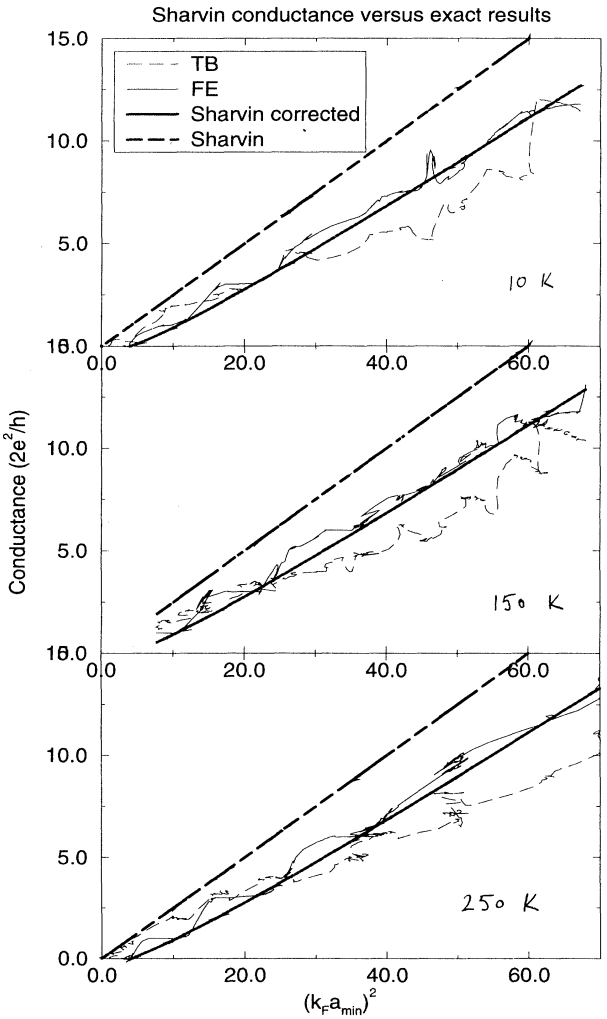

FIG. 12. The calculated free-electron and tight-binding conductances versus $(k_F a_{\min})^2$, for each temperature. k_F is the Fermi wave vector and $a_{\min}$ is the effective minimal contact radius. The Sharvin conductance, $G_S = (k_F a_{\min})^2/4$, and the corrected Sharvin conductance, $G=(k_F a_{\min})^2/4-(k_F a_{\min})/2$, are also plotted for comparison.

at the boundaries of the contact (for example, see Ref. 29), shows that in the case of a perfectly uniform jellium constriction of cross-sectional area A and corresponding perimeter P, in the semiclassical limit $Ak_F^2 \gg 1$ the right result for the conductance [Eq. (19)] is

$$G = G_0 \left(\frac{Ak_F^2}{4\pi} - \frac{Pk_F}{4\pi} \right) \tag{20}$$

(up to a negligible constant term), where the leading term gives G_S. This result holds for circular and for rectangular constrictions and probably holds for constrictions of any cross-sectional shape.

The corrected Sharvin conductance from Eq. (20) is also plotted in Fig. 12. It is clearly seen that the corrected conductance given by Eq. (20) is much closer to the present exact FE results than the Sharvin limit is.

Interestingly, the TB conductances in Fig. 12 generally lie below the semiclassical jellium estimate from Eq. (20) and below the exact calculated FE conductance values. The principal reason for this is the difference between the FE and TB dispersion relations. The general statement that the zero-temperature conductance, in units of G_0, for a perfectly uniform and homogeneous constriction with a given electron density is equal to the number of open channels at the Fermi energy, is true regardless of the precise energy-momentum dispersion relation. This is so because the contribution of each channel contains a product of the corresponding longitudinal density of states and longitudinal group velocity at the Fermi energy, and this product is equal to the same constant for any dispersion relation. However, the actual *number* of open channels for a given electron density does depend, albeit not very strongly, on the dispersion relation (or, in other words, on the effective Fermi momentum).

A further reason for the suppression of the TB conductances relative to the jellium ones is that there are more sources of backscattering in the TB model than in the FE one. This backscattering has the effect of reducing the contribution to the conductance of the open channels themselves, and is also responsible for the breakdown of conductance quantization.

In order to obtain a realistic general calibration curve relating the conductance to the actual cross-sectional area of the contact, we have taken the average of the calculated FE and TB conductances. The average conductances for all three temperatures are plotted versus $(k_F a_{\min})^2$ in Fig. 13, together with the jellium Sharvin limit. At least for the range of minimal cross sections studied here, we see a linearlike dependence of the average conductance on $(k_F a_{\min})^2$. This linear dependence is the same for all three temperatures (the bold solid line in Fig. 13) and has a slope which is considerably smaller than the one in the Sharvin limit. From our calculations we obtain the fit

$$G_{\text{fit}} = G_0 (k_F a_{\min})^2 / 5.8. \tag{21}$$

The essential parameter in this formula is the minimal cross-sectional *area* of the contact and one can expect the result to be fairly insensitive to the shape of the contact cross section.

We hope that the above approximate formula will be of practical use in the analysis of real geometries in experiments on atomic-scale contacts.

D. Possibilities for further research

There are a number of ways in which the present calculations may be extended and refined. The assumed cylindrical symmetry of the contact in the FE calculation is an approximation which can in principle be removed. The TB model can be extended by the inclusion of further orbitals and by a systematic study of the importance of the scaling of the hopping integrals with distance.

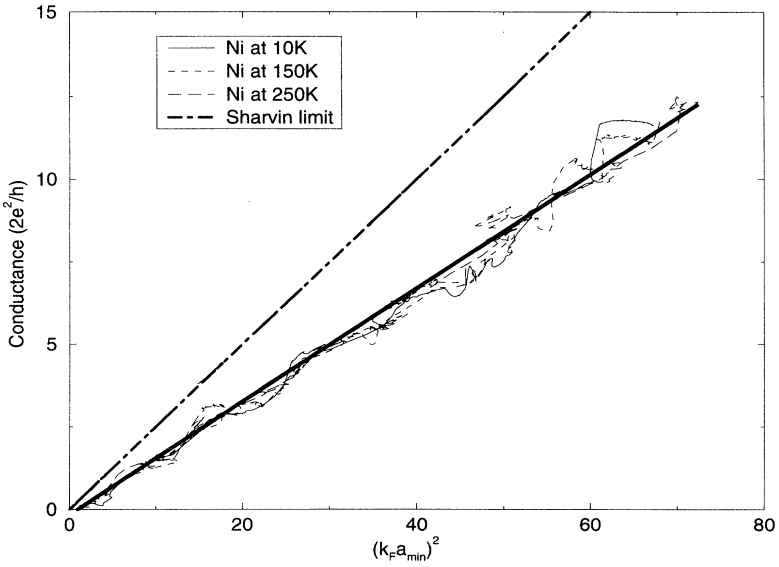

FIG. 13. The average of the tight-binding and the free-electron conductances versus $(k_F a_{\min})^2$, for each temperature. k_F is the Fermi wave vector and $a_{\min}$ is the effective minimal contact radius. The average conductances at all three temperatures follow a common trend. The Sharvin limit, $G_S = (k_F a_{\min})^2/4$, is also plotted for comparison.

In our view, however, the most interesting extension of the current calculations will consist in the inclusion of self-consistency. In the near future, we intend to do TB calculations with the imposition of local charge neutrality (LCN) on each atom in the contact. Since the coordination number of the atoms in the constriction can be very different from that of atoms in the bulk, LCN should give rise to significant on-site energy corrections for the constriction atoms. These on-site energy shifts are likely to have a significant effect on the calculated conductance.

ACKNOWLEDGMENTS

The authors wish to thank J.M. Krans, C.J. Muller, J.B. Pethica, S.N. Rashkeev, and J.M. van Ruitenbeek for many stimulating discussions. The research for this paper was carried out in the Materials Modelling Laboratory at Oxford University, which is partially funded by the EPSRC under Grant No. GR/H/58278.

APPENDIX: RELATION BETWEEN THE TIGHT-BINDING AND FREE-ELECTRON MODELS

It is instructive to establish a connection between the continuous free-electron and the discrete tight-binding formalisms. They both yield solutions to the scattering problem of electron propagation through ballistic constrictions and are fundamentally related to each other. As discussed in the text, both models allow size quantization of the conductance. To see more precisely the correspondence between the two, let us consider a perfect periodic crystal described by the tight-binding Hamiltonian

$$H = \sum_{\mathbf{m}} \epsilon_{\mathbf{m}} c^{\dagger}_{\mathbf{m}} c_{\mathbf{m}} - \sum_{\langle \mathbf{mn} \rangle} t_{\mathbf{mn}} c^{\dagger}_{\mathbf{m}} c_{\mathbf{n}}, \tag{A1}$$

where $\langle \mathbf{mn} \rangle$ denotes the corresponding pair of neighboring atoms. Now we cast it into continuous form[30] by introducing the field operators

$$\hat{\psi}(\mathbf{r}) = \frac{1}{N^{1/2}} \sum_{\mathbf{m}} \delta(\mathbf{r} - \mathbf{m}) c_{\mathbf{m}}, \tag{A2}$$

and rewrite the Hamiltonian from Eq. (A1) as

$$\hat{H} = \int d^3r \; \epsilon(\mathbf{r}) \hat{\psi}^{\dagger}(\mathbf{r}) \hat{\psi}(\mathbf{r}) + \int d^3r d^3r' \; \hat{\psi}^{\dagger}(\mathbf{r}) t(\mathbf{r} - \mathbf{r}') \hat{\psi}(\mathbf{r}'), \tag{A3}$$

where

$$t(\mathbf{r} - \mathbf{r}') = \sum_{\mathbf{k}} t_{\mathbf{k}} \exp[i\mathbf{k} \cdot (\mathbf{r} - \mathbf{r}')], \tag{A4}$$

$$t_{\mathbf{k}} = \sum_{m \neq 0} t(\mathbf{m}) \exp(-i\mathbf{k} \cdot \mathbf{m}). \tag{A5}$$

We can also include the effects of an external magnetic field. In the presence of a vector potential $\mathbf{A}$, the hopping integral changes in the following way:

$$t(\mathbf{m} - \mathbf{m}') \rightarrow t(\mathbf{m} - \mathbf{m}') \exp\left[i \frac{e}{\hbar} \mathbf{A} \cdot (\mathbf{m} - \mathbf{m}') \right]. \tag{A6}$$

That gives us the hopping integral in real space,

$$t(\mathbf{r} - \mathbf{r}') = \sum_{\mathbf{k}} t_{\mathbf{k} - \frac{e}{\hbar}\mathbf{A}} \exp[i\mathbf{k} \cdot (\mathbf{r} - \mathbf{r}')]. \tag{A7}$$

Expanding $t_{\mathbf{k} - \frac{e}{\hbar}\mathbf{A}}$ about $\mathbf{k} - \frac{e}{\hbar}\mathbf{A} = 0$ and keeping only the first two terms we obtain

$$t(\mathbf{r} - \mathbf{r}') = \left[t_0 + \frac{1}{2m} (-i\hbar\nabla - e\mathbf{A})^2 \right] \delta(\mathbf{r} - \mathbf{r}'), \tag{A8}$$

where

$$\frac{1}{m} = \frac{1}{\hbar^2} \left(\frac{\partial^2 t_k}{\partial k^2} \right)_{k \rightarrow 0}. \tag{A9}$$

Thus, as may be expected physically, the discrete model reduces to the continuous one in the limit of large wavelengths, or, conversely, in the limit of small lattice spacings. The estimate (A8) is valid whenever the band is approximately parabolic. It is important to note that in the case of a half-filled band and/or in the proximity of the van Hove singularities the correspondence between the TB and the FE models is the worst. In the case of a half-filled band, the Fermi surface and, correspondingly, the Fermi momentum are largest. In this case the parabolicity of the band can be easily lost. The effect of the van Hove singularities could also make the results of the models quite different.

It is also interesting to observe that Eqs. (A8) and (11) provide a prescription of how to renormalize approximately the transverse hopping integrals for a system with rough boundaries so as to reduce the problem to that of a system with smooth boundaries. This type of procedure may be useful for making approximate estimates of the effects of roughness, but it has not been used in the present work.

[1] C.J. Muller, J.M. van Ruitenbeek, and L.J. de Jongh, Physica C **191**, 485 (1992).
[2] C.J. Muller, J.M. van Ruitenbeek, and L.J. de Jongh, Phys. Rev. Lett. **69**, 140 (1992).
[3] L. Olesen, E. Laegsgaard, I. Stensgaard, F. Besenbacher, J. Schiøtz, P. Stoltze, K.W. Jacobsen, and J.K. Nørskov, Phys. Rev. Lett. **72**, 2251 (1994).
[4] N. Agraït, J.G. Rodrigo, and S. Vieira, Phys. Rev. B **47**, 12 345 (1993).
[5] J.I. Pascual, J. Méndez, J. Gómez-Herrero, A.M. Baró, and

N. García, Phys. Rev. Lett. **71**, 1852 (1993).
[6] T.N. Todorov and A.P. Sutton, Phys. Rev. Lett. **70**, 2138 (1993).
[7] J.M. Krans, C.J. Muller, I.K. Yanson, Th.C.M. Govaert, R. Hesper, and J.M. van Ruitenbeek, Phys. Rev. B **48**, 14 721 (1993).
[8] J.M. Krans, C.J. Muller, N. van der Postma, A.P. Sutton, T.N. Todorov, and J.M. van Ruitenbeek, Phys. Rev. Lett. **74**, 2146 (1995).
[9] J.M. Krans and J.M. van Ruitenbeek (private communication).
[10] C.J. Muller, J. M. Krans, T.N. Todorov, and M.A. Reed, Phys. Rev. B (to be published).
[11] A.P. Sutton and J. Chen, Philos. Mag. Lett. **61**, 139 (1990).
[12] M.P. Allen and D.J. Tildesley, *Computer Simulation of Liquids* (Oxford University Press, Oxford, 1987).
[13] A.P. Sutton, J.B. Pethica, H. Rafii-Tabar, and J.A. Nieminen, in *Electron Theory in Allow Design*, edited by D.G. Pettifor and A.H. Cottrell (Institute of Materials, London, 1992), Chap. 7.
[14] T.N. Todorov, G.A.D. Briggs, and A.P. Sutton, J. Phys. Condens. Matter **5**, 2389 (1993).
[15] R. Landauer, IBM J. Res. Dev. **1**, 223 (1957); Y. Imry, in *Directions in Condensed Matter Physics*, edited by G. Grinstein and G.F. Mazenko (World Scientific, Singapore, 1986), p. 101.
[16] D.S. Fisher and P.A. Lee, Phys. Rev. B **23**, 6851 (1981).
[17] J. Mašek and B. Kramer, Z. Phys. B **75**, 37 (1989).
[18] E. Tekman and S. Ciraci, Phys. Rev. B **43**, 7145 (1991).
[19] E.N. Bogachek, A.N. Zagoskin, and I.O. Kulik, Fiz. Nizk. Temp. **16**, 1404 [Sov. J. Low Temp. Phys. **16**, 796 (1990)].
[20] A.M. Bratkovsky and S.N. Rashkeev (unpublished).
[21] B.J. van Wees, H. van Houten, C.W.J. Beenakker, J.G. Williamson, L.P. Kouwenhoven, D. van der Marel, and C.T. Foxon, Phys. Rev. Lett. **60**, 848 (1988); D.A. Wharam, M. Pepper, H. Ahmed, J.E.F. Frost, D.G. Hasko, D.C. Peacock, D.A. Ritchie, and G.A.C. Jones, J. Phys. C **21**, L209 (1988).
[22] L.I. Glazman, G.B. Lesovik, D.E. Khmelnitskii, and R.I. Shekhter, Pis'ma Zh. Eksp. Teor. Fiz. **48**, 218 (1988) [JETP Lett. **48**, 238 (1988)]; L.I. Glazman and M. Jonson, Phys. Rev. B **44**, 3810 (1991).
[23] A. Brataas and K.A. Chao, Mod. Phys. Lett. **7**, 1021 (1993).
[24] A.M. Zagoskin and R.I. Shekhter, Phys. Rev. B **50**, 4909 (1994).
[25] S.A. Gurvitz and Y.B. Levinson, Phys. Rev. B **47**, 10 578 (1993).
[26] L. Olesen, E. Laegsgaard, I. Stensgaard, F. Besenbacher, J. Schiøtz, P. Stoltze, K.W. Jacobsen, and J.K. Nørskov, Phys. Rev. Lett. **74**, 2147 (1995).
[27] Yu.V. Sharvin, Zh. Eksp. Teor. Fiz. **48**, 984 (1965).
[28] J.A. Torres, J.I. Pascual, and J.J. Sáenz, Phys. Rev. B **49**, 16 581 (1994).
[29] P.M. Morse and H. Feshbach, *Methods of Theoretical Physics* (McGraw-Hill, New York, 1953), Chap. 6, Sec. 3.
[30] A.S. Alexandrov and N.F. Mott, *High-Temperature Superconductors and Other Superfluids* (Taylor and Francis, London, 1994), Chap. 5, p. 95.